Modeling study on the influence of the pressure on a dielectric barrier discharge microplasma†

T. Martens,[a] A. Bogaerts,*[a] W. J. M. Brok[b] and J. J. A. M. van der Mullen[b]

Received 2nd April 2007, Accepted 6th June 2007
First published as an Advance Article on the web 22nd June 2007
DOI: 10.1039/b704903j

In this paper we present a one-dimensional fluid model to study the properties of very small dielectric barrier discharges (DBD), which can be used as microchip plasma sources for analytical spectrometry. The influence of the pressure on this kind of discharge was investigated to obtain more insight in the variations of discharge current and the differences in particle densities that arise when operating at different pressures. The studied discharge gas is helium and is described with passive He background atoms, He^+ and $He_2{}^+$ ions, He metastable atoms, higher excited states of He, $He_2{}^*$ excimers and electrons. We show that the plasma activity, expressed in discharge current, is remarkably higher for pressures ranging from 50 to 140 mbar. For most pressures the calculated maximum current density is about 0.1 A cm^{-2}, whereas in the range from 50 to 140 mbar the maximum current density is about 0.3 A cm^{-2}. We also report how the plasma densities alter at different operating pressures, with spatially averaged densities at maximum current ranging from about 10^{16} m^{-3} to 10^{18} m^{-3}, depending on the plasma species, and identify the main underlying processes, which are responsible for these evolutions.

1. Introduction

Miniaturization of analytical plasma devices is currently a major subject of research, especially if these devices can be operated on microchips. Such small plasma devices require a smaller amount of both sample and carrier gas and therefore they can eventually be used to construct a portable device. Moreover if the amount of sample that has to be measured is large, multiple parallel measuring devices can be constructed, which considerably reduces the time cost.

The ultimate goal of this miniaturization process is the construction of a single chip with all the necessary steps for sample preparation integrated. If such a lab-on-the-chip can be constructed, the analytical tool becomes more mobile and it makes it more interesting to be mass produced, which subsequently lowers the cost of this analytical instrument.

There are a lot of configurations that can be used to generate such microplasmas, ranging from direct current discharges, capacitively coupled radio frequency discharges and microwave discharges to miniature inductively coupled discharges, liquid-sampling atmospheric pressure glow-discharges and dielectric barrier discharges.[1–6] Nice overviews and descriptions of these different analytical microplasmas can be found in ref. 7–9

In this framework of miniaturization, Niemax, Franzke and coworkers have developed a microdischarge in a dielectric barrier configuration.[6,10–12] A dielectric barrier discharge (DBD) or silent discharge is a plasma generated with at least one of the electrodes screened using an electrical insulator or dielectric. This inhibits the flowing of a conduction current from one electrode to the other and necessitates the use of an alternating voltage. The operating frequencies range from a few Hz up to a few MHz, but mostly they are in the kHz range. DBDs are often operated at atmospheric pressure,[13] but they can also be sustained at lower pressure. DBDs are already widely used as plasma display discharge cells, for industrial ozone generators and in surface treatments.[14–17]

2. Description of the model

The 2-dimensional fluid model used in this paper was originally developed for the numerical description of the discharge cells used in plasma display technology.[18,19] This model has been further developed by Brok and van Dijk[20] and has been applied to other kinds of discharges like the breakdown phenomena in fluorescent lamps,[20,21] dielectric barrier discharges at low pressure (400 Pa)[22] and also for the modeling of microdischarge DBDs used for analytical applications.[23]

2.1 The fluid model

The fluid model employed in this work is, like similar fluid models used for the description of low temperature plasmas,[24–28] based on the iterative and time dependent solution of the continuity equations for the particle density n_p of both heavy particles (*i.e.* different ions and neutral species) and the electrons

$$\frac{\partial n_p}{\partial t} + \nabla \cdot \mathbf{J}_p = S_p \qquad (1)$$

and the continuity equation of the electron energy density for which we define $w_e = n_e\bar{\varepsilon}$ with $\bar{\varepsilon}$ as the mean electron energy

[a] *Department of Chemistry, University of Antwerp, Universiteitsplein 1, B-2610 Wilrijk, Belgium. E-mail: annemie.bogaerts@ua.ac.be*
[b] *Department of Applied Physics, Eindhoven University of Technology, P.O. Box 513, 5600 MB Eindhoven, The Netherlands*
† Presented at the 2007 European Winter Conference on Plasma Spectrochemistry, Taormina, Italy, February 18–23, 2007.

$$\frac{\partial w_e}{\partial t} + \nabla \cdot \mathbf{J}_{w_e} = -e\mathbf{J}_e \cdot \mathbf{E} + S_{w_e} \quad (2)$$

In these equations S_p is the particle source term accounting for the creation and destruction of particle p due to chemical reactions and S_{w_e} is the source term of the electron energy density representing the loss and gain of the electron energy due to collisions. The first term on the right hand side of eqn (2), which contains the electron charge $-e$, accounts for the Ohmic heating of the electrons due to the electric field. The fluxes **J** in the above equations are described using the drift-diffusion approach which leads to the equations

$$\mathbf{J}_p = \pm\mu_p n_p \mathbf{E} - D_p \nabla n_p \quad (3)$$

and

$$\mathbf{J}_{w_e} = -\frac{5}{3}\mu_e w_e \mathbf{E} - \frac{5}{3} D_e \nabla w_e \quad (4)$$

for the particle flux and the electron energy density flux, respectively. μ_p and D_p are the electric mobility and the diffusion coefficient of particle p, respectively. **E** is the electric field calculated from the Poisson equation

$$\nabla \cdot (\mathbf{E}\varepsilon_m) = \rho \quad (5)$$

in which ε_m is the permittivity of the medium (used both for plasma and the dielectric) and ρ is the space charge density. The continuity equations are only solved in the discharge gap, but the Poisson equation is also solved within the dielectrics. At the interface of the dielectric with the discharge gas, Gauss' law is used to account for the surface charges accumulated on the dielectric surface.

In our model, the density and the temperature of the background gas are assumed constant, both in time and in space. The mobility of the electrons and a large part of their collisional reactions are described as parameters depending on the electron mean energy. These dependencies are calculated using the external Boltzmann solver Bolsig+,[29] which creates look-up tables for the mean electron energy, the electric mobilities and the reaction rate coefficients as a function of the reduced electric field. Consequently, the electric mobilities and the reaction rate coefficients can be used as a function of the electron energy. The electron diffusion coefficients are derived using the Einstein relation.

For the ions, the local field approximation is used. The mobilities of He^+ and He_2^+ in helium gas are found in ref. 30 as tabulated versus the reduced electric field. From these values the diffusion coefficients are calculated using the Einstein relation.

Scaled diffusion coefficients for the neutral particles are calculated from the Chapman–Enskog equation for binary gas systems,[31] using characteristic Lennard–Jones energies and lengths found in ref. 31 and 32. The calculated coefficients are 0.24 $m^2\ s^{-1}$ mbar for He_m^* and He^{**} and 0.16 $m^2\ s^{-1}$ mbar for He_2^*.

A more detailed description of the physics used in the model as well as a description of the numerical methods applied to solve these equations can be found elsewhere.[18,20]

2.2 Chemical input

2.2.1 Chemical species. In order to solve eqn (1) and eqn (2) it is necessary to have a consistent set of chemical reactions, which describe the loss and creation of particles as well as the loss or gain of electron energy due to collisions. Table 1 contains all the chemical reactions and reaction rate coefficients used in the present model. The same species and reaction set have previously been applied in ref. 23. For the description of the He chemistry we used, besides the electrons and the He ground state atoms, 5 distinct types of He species, namely, the singly charged ion He^+, the singly charged molecule He_2^+, two excited states He_m^* and He^{**} and the excimer molecule He_2^*. The excited state He_m^* is a compound state consisting of the two metastable levels He(2^3S) and

Table 1 Complete set of reactions used in the model with their reaction rate coefficients. The first reaction accounts for the elastic energy losses of the electrons due to collision with He background gas atoms. The first five reactions are all accounts for using energy dependent cross sections

No.	Reaction	Reaction coefficient	Ref.
0	$e^- + He \rightarrow e^- + He$	$k = f(\sigma(\bar{\varepsilon}))$	35
1	$e^- + He \rightarrow e^- + He_m^*$	$k = f(\sigma(\bar{\varepsilon}))$	35
2	$e^- + He \rightarrow e^- + He^{**}$	$k = f(\sigma(\bar{\varepsilon}))$	35
3	$e^- + He \rightarrow 2\,e^- + He^+$	$k = f(\sigma(\bar{\varepsilon}))$	35
4	$e^- + He_m^* \rightarrow 2\,e^- + He^+$	$k = f(\sigma(\bar{\varepsilon}))$	35
5	$e^- + He_m^* \rightarrow e^- + He$	$k = 2.9 \times 10^{-15}\ m^3\ s^{-1}$	37, 39
6	$e^- + He_m^* \rightarrow e^- + 2\,He$	$k = 3.8 \times 10^{-15}\ m^3\ s^{-1}$	37
7	$He^+ + 2\,e^- \rightarrow He_m^* + e^-$	$k = 6.0 \times 10^{-32}\ m^6\ s^{-1}$	37
8	$He_2^+ + 2\,e^- \rightarrow He_m^* + He + e^-$	$k = 2.8 \times 10^{-32}\ m^6\ s^{-1}$	37
9	$He_2^+ + e^- + He \rightarrow He_m^* + 2\,He$	$k = 3.5 \times 10^{-39}\ m^6\ s^{-1}$	37
10	$He_2^+ + 2\,e^- \rightarrow He_2^* + e^-$	$k = 1.2 \times 10^{-33}\ m^6\ s^{-1}$	37
11	$He_2^+ + e^- + He \rightarrow He_2^* + He$	$k = 1.5 \times 10^{-39}\ m^6\ s^{-1}$	37
12	$He^{**} + He \rightarrow He_2^+ + e^-$	$k = 1.5 \times 10^{-17}\ m^3\ s^{-1}$	27
13	$He_m^* + He_m^* \rightarrow He_2^+ + e^-$	$k = 2.0 \times 10^{-15}\ m^3\ s^{-1}$	37, 39
14	$He_m^* + He_m^* \rightarrow He^+ + He + e^-$	$k = 8.7 \times 10^{-16}\ m^3\ s^{-1}$	37, 39
15	$He^+ + 2\,He \rightarrow He_2^+ + He$	$k = 6.5 \times 10^{-44}\ m^6\ s^{-1}$	37
16	$He_m^* + 2\,He \rightarrow He_2^* + He$	$k = 1.9 \times 10^{-46}\ m^6\ s^{-1}$	37
17	$He_m^* + He_2^* \rightarrow He^+ + 2\,He + e^-$	$k = 5.0 \times 10^{-16}\ m^3\ s^{-1}$	37
18	$He_m^* + He_2^* \rightarrow He_2^+ + He + e^-$	$k = 2.0 \times 10^{-15}\ m^3\ s^{-1}$	37
19	$He_2^* + He_2^* \rightarrow He^+ + 3\,He + e^-$	$k = 3.0 \times 10^{-16}\ m^3\ s^{-1}$	37
20	$He_2^* + He_2^* \rightarrow He_2^+ + 2\,He + e^-$	$k = 1.2 \times 10^{-15}\ m^3\ s^{-1}$	37
21	$He_2^* + He \rightarrow 3\,He$	$k = 4.9 \times 10^{-22}\ m^3\ s^{-1}$	27

$He(2^1S)$. The excited state He^{**} represents the higher excitation levels lumped together. This approach is similar to the approach used by Rauf and Kushner[33] for the description of a plasma display panel discharge cell, only we use two excited states instead of one. The use of both a lower and a higher excited compound state has also previously been applied, albeit not for He, but for an Ar discharge.[34] We chose this approach because it provides a small correction for the electron energy loss due to collisions with He atoms and moreover the He^{**} particle is the source for the Hornbeck–Molnar associative ionization (reaction 12 in Table 1). In section 3.2 of this paper it will be shown that the Hornbeck–Molnar associative ionization actually becomes very dominating in the discharge, since it becomes the main production process for the two most important charge carriers in the discharge, namely the electrons and the He_2^+ molecular ions.

2.2.2 Chemical reactions. The rates of the production and loss processes of the different plasma species are calculated in the model from the densities of the colliding particles and the associated reaction rate coefficients (summarized in Table 1). For the first five reactions, an energy dependent reaction rate coefficient is used. These coefficients are calculated using the previously mentioned Boltzmann solver[29] with the collision cross sections found in ref. 35 and 36 as input. The electron impact de-excitation and dissociation reactions, *i.e.* reactions 5 and 6 in Table 1, are treated as independent of the electron energy. This independence is one of the experimental results in the detailed study of the elementary processes in high-pressure He of Deloche *et al.*[37] Since we based most of our chemical description on their study, we tried to stay as consistent with their results as possible. With respect to the excited states, our main interest is in the particles with longer lifetimes (*i.e.* He_m^* and He_2^*) since they are considered the most important in determining the plasma properties.[27,28,33,38] He_m^* and He_2^* can also be excited to a radiative level and undergo radiative relaxation, but we did not consider these processes, because the superelastic de-excitation (*i.e.* reactions 5 and 6) is a much more efficient process for destroying metastables. Indeed Deloche *et al.*[37] used these superelastic reactions to express the overall destruction of the metastables due to electron collisions, and they calculated the reaction rate coefficients for these reactions. Moreover, the radiative decay of He_m^* is not a very efficient process since reabsorption of the emitted light has a very high probability. This puts nearly all the bound electrons, which were initially excited from their metastable level to a radiative state, back in their original states. For He_2^* this is of course not the issue since its molecular ground state is dissociative.[37]

The experimental conditions of the research on which we based our reaction rate coefficients are high pressure helium afterglow studies.[37,39] The plasmas investigated in these studies are in the pressure range of 6 to 130 mbar, which is comparable with our pressure range from 25 mbar to 1.1 bar, but since they are afterglow discharges, they have a low to zero power transfer, while the discharges investigated in this study have calculated power transfers of tens of mW. Therefore we added the first five electron reactions in Table 1 (as mentioned above). The afterglow also causes the densities of the excited species to be low and hence the possibility arises that reactions induced by excited states are underestimated, as is also mentioned in these studies. Therefore we make use of the additional reactions 12 and 21, *i.e.* the Hornbeck–Molnar associative ionization and the He atom induced dissociation respectively, to account for this effect. This is consistent with previous research in high pressure helium discharges, in which these reactions were found to be non-negligible.[27]

2.3 Model specifications

In the present paper our main interest is to study the influence of the pressure on the possibility of stable discharge operation, on the electric current and on the densities of the active plasma species under the conditions of a dielectric barrier microdischarge.

For this purpose we chose to use a one-dimensional model, because such a model only uses the effects such as the gap width and the barrier thickness, which makes us able to study the pressure influence independently from the two and three-dimensional effects. A one-dimensional model is indeed suitable for such purpose, but it makes comparison with the experiment difficult, since the difference with the experimental situation becomes much greater. The electrodes used in the experiments are 50 mm long and 800 μm wide,[6] which is long and narrow, as is also the discharge channel through which the plasma is transported. Experimentally, this causes a considerable amount of particles to be lost at the sides. The influence of the side walls is an important parameter in discharge stability, since it lowers the density of charge carriers in the discharge. This effect is not accounted for in one-dimensional simulations and would, in this case, require a three-dimensional approach. For our present purposes, a one-dimensional model is more suitable and also much less computationally expensive than a three-dimensional model. Therefore, we were able to use a very simple geometry for our model that requires a two-dimensional geometrical input.

We chose a geometry with axial symmetry consisting of 104 cells in the axial direction and three cells in the radial direction, so we basically had a one-dimensional model. For some test-cases we implemented more cells in the radial direction to check for variations, but in the applied ranges no variation was observed.

The applied grid was equidistant in both radial and axial direction and every grid distance was 10 μm. Of these 104 axial cells, two on every end are electrodes, of which on one end the electrode is grounded and on the other a voltage is applied. Moving more to the middle, two cells on every end are dielectric and the remainder in between is discharge gas. This geometry is similar to the dielectric barrier microdischarge studied by Miclea and Kunze,[6,10–12] where also a gap of 1 mm between the electrodes, including the dielectrics, is studied and where each dielectric has a thickness of 20 μm.

The experimentally used dielectrics are made of glass, therefore we used a dielectric constant of $\varepsilon_r = 9$. Similar to ref. 19, we used a secondary electron emission coefficient of 0.2 for the atomic and molecular helium ions and considered that the produced secondary electrons have an initial energy of 5 eV.

As mentioned above, the gas temperature in the model is assumed constant in time and space. Experimental data on the gas temperature in this He microdischarge were not directly available, therefore we chose to use a gas temperature of 300 K.

For the ignition of the dielectric barrier discharge we applied a rectangular voltage pulse of 750 V peak-to-peak and a frequency of 5 kHz with a rise-time of 2 μs, as is reported in ref. 10.

3. Results and discussion

The main goal of this paper is to clarify the influences of the operating pressure on discharge characteristics, such as the electric current, particle densities, and the identification of the governing processes occurring in this kind of configuration. Since the electric properties of the DBD are very characteristic, and the amplitudes and widths of the current peaks tell us a lot about the discharge, these will be the first to be discussed.

3.1 Electrical properties

Fig. 1 shows the calculated electrical characteristics of the helium DBD operated at 87 mbar. The parameter T on the bottom axis is the duration in time of half a period, hence $2T$ = 200 μs. In the top frame the rectangular applied voltage is shown together with the potential difference across the discharge gap or so-called gap voltage. The latter is determined both by the potentials applied to the electrodes and by the charging effects which occur on the dielectrics. In the bottom frame the calculated current density is shown. The graph shows that the helium discharge event occurs once every half period when the gap voltage has reached a value of about 360 V and it causes a maximum current density of 280 mA cm^{-2}. This rather high value is due to the overvoltage in the gap-voltage that occurs in the simulation. It is reported in ref. 40 that even a small overvoltage in a dielectric barrier discharge in He can cause the electric current densities to become 100 times larger than in the situation where the breakdown voltage is only just reached. The breakdown voltage of He at this pressure and discharge gap is about 220 V.[41] The gap voltage that can be seen in Fig. 1 is 364 V. This means that there is a significant overvoltage. In the case of sinusoidal applied voltages, such an overvoltage leads to a multipeak discharge, as in ref. 25 and 42. In the case of a rectangular voltage, the voltage rise is too fast for multiple discharges to be formed and the amplitude of the current peak rises significantly.

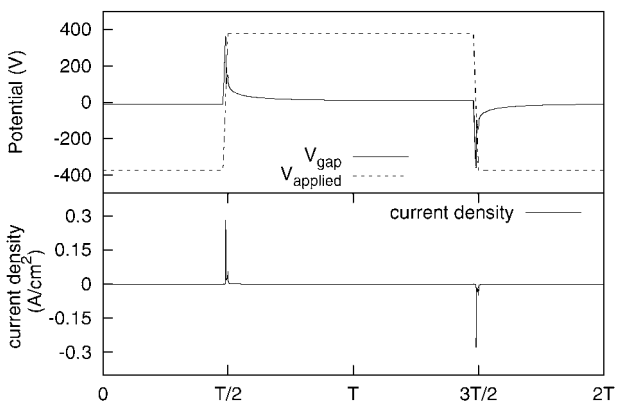

Fig. 1 Voltage applied to the electrodes (top frame, dotted line), and potential difference between the surfaces of the dielectrics, also called gap voltage (top frame, solid line). The current density peak, shown in the bottom frame, always occurs right after the maximum in gap voltage. This profile is taken for a pressure of 87 mbar and the current density peaks have an amplitude of 0.28 A cm^{-2}.

The value of 87 mbar has been chosen, because it lies right in between the values of 10 and 180 mbar of which it is reported in ref. 6 that "any kind of noble gas with a pressure value in that range can be ignited and sustained in this kind of experimental configuration". In this study of the influence of the pressure, we have simulated far beyond this range. With the present model, we were able to simulate periodic plasma behavior within the range of about 15 mbar to about 1.1 bar in helium. The origins of these pressure limits are discussed in section 3.3. Outside this range, the model was not able to sustain a large enough amount of charge carriers and therefore no periodic steady state was reached. The presented results are taken within a safe range of 25 to 1100 mbar to avoid the influences of possible instabilities due to pressure.

The obtained results at different pressures did not always show symmetric behavior regarding both halves of the period. In Fig. 2 we show in the top frame the peak values of J_+ and J_-, which are the positive and negative current density peaks, respectively. For the pressures investigated, the current density profiles were similar to Fig. 1 of the 87 mbar discharge, considering the manifestation of a single narrow current peak every half period. Differences in the profiles are only seen in the peak amplitudes and in the symmetry of the peaks. Therefore, the ratio of the positive to the negative peak values is shown in the bottom frame of Fig. 2.

For most of the pressures investigated, a discharge symmetric in time has been predicted with the model. At 25 and 37 mbar however an asymmetric discharge has been obtained, with a higher negative than positive peak. Moreover, on the

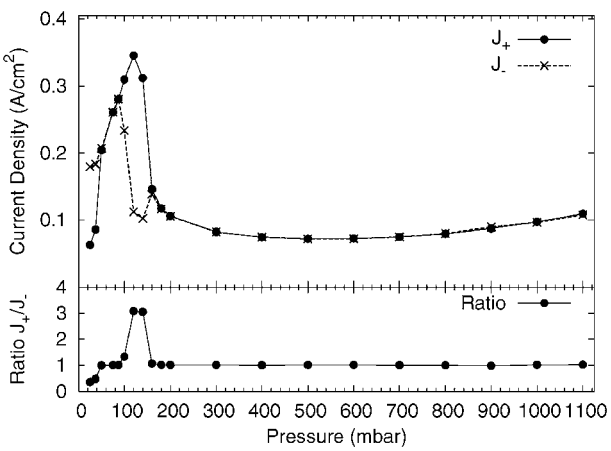

Fig. 2 Influence of the pressure on the discharge current density. In the top frame the absolute values of the positive and negative current peaks (J_+ and J_-, respectively) are plotted at different pressures. In the bottom frame the absolute value of the ratio of the positive to the negative current peak is shown. There is clearly a higher current density in the region from 50 to 140 mbar, where also the positive current peak seems to be significantly higher than the negative.

other hand, at pressures from 100 to 140 mbar the negative peak was found to be lower than the positive peak. The reason for this asymmetry is not clear. This is probably due to the spatial differences in the reaction rates, but this is beyond the scope of this paper, since we are mainly considering the spatially averaged properties.

Interesting to remark, is that the current density in the helium plasma seems to be considerably higher in the range from 50 to 140 mbar, which is similar to the typical operating pressures from 10 to 180 mbar reported in ref. 6. This higher current density is, as is shown later in section 3.2, associated with significantly higher charged particle densities, which indicates that the plasma may possess increased dissociative capabilities, or plasma "activity". The reason for this activity will be discussed further in section 3.2. This result is interesting for the use of this plasma in diode laser atomic absorption spectrometry, as is suggested in ref. 6, since the purpose of the plasma is the dissociation of molecules and excitation of atoms, which are processes that are determined by this activity.

To obtain an idea of the plasma regimes that are reached in the high current and low current density zone, a comparison of the spatial potential distribution and the densities of the charged particles is made in Fig. 3 for the two distinct pressures of 120 mbar and 500 mbar. These pressures are chosen because 120 mbar is the pressure with the highest current density and 500 mbar is the pressure above 120 mbar with the lowest current density, as can be seen in Fig. 2. The positive ion density distributions shown in Fig. 3 are, of course, the sum of the densities of He^+ and $He_2{}^+$. These spatial distributions are taken at the moment immediately after the positive current peak, because the potential distribution needs a fraction of time (about 0.25 μs in the model) to adapt itself to the newly formed charges (see ref. 23 for more details).

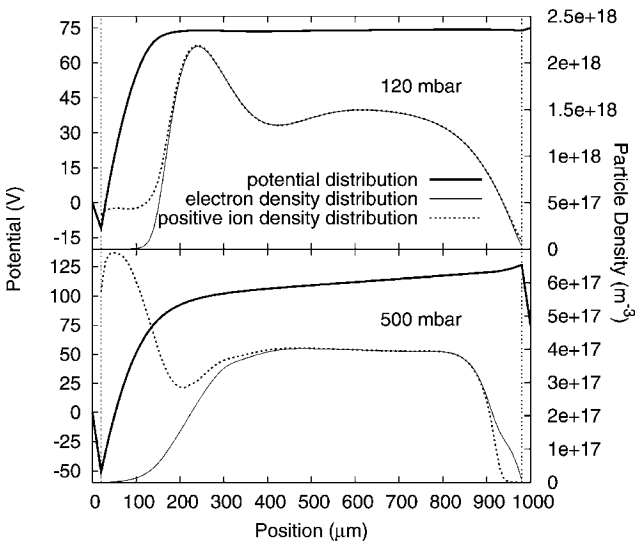

Fig. 3 Calculated spatial distributions of the voltage profile, the electron density and the sum of positive ion densities for two distinct cases of 120 mbar and 500 mbar. The grounded electrode is at the left hand side and the powered electrode at the right, which is currently at a positive potential. From 0 to 20 μm and from 980 to 1000 μm there is no discharge gas, since the space is filled with dielectric. Hence the particle densities in those regions are zero. The vertical dotted lines denote the border between plasma and dielectrics.

These spatial profiles are typical for dielectric barrier discharges as can be seen in ref. 25 and 43, where the density profiles of the charged particles in the vicinity of the dielectric are even more narrow because of the atmospheric pressure. The reason that the electron density in the 500 mbar case is not as high in the vicinity of the dielectric as in the 120 mbar case lies in the very fast profile variation at maximum current in this kind of configuration, as is also reported in ref. 23. The electron profile in the 500 mbar case has already moved slightly away from the dielectric.

Important observable features are the positive charges near the grounded (*i.e.* most negative) electrode, where the densities are large enough to form a sheath, and the quasi-neutrality in the center of the plasma, which forms a plasma-bulk. In the 500 mbar profile, there is also a small excess of electrons near the powered (*i.e.* most positive) electrode which causes a small rise in the potential profile, which is not observed in the 120 mbar case. These sheath and bulk formations, even with the possibility of a small electron excess near the powered electrode, are typical characteristics of the glow discharge regime.[44,45]

In Fig. 3 there is also a very interesting difference in the densities of the charged particles. The densities in the plasma at 120 mbar are about 3 to 3.5 times as large as in the 500 mbar plasma. This was of course to be expected, since it can be seen in Fig. 2 that the current density at 120 mbar, which is the peak value, is also about 3.5 times as large as the current density in the 500 mbar plasma.

The behavior of the neutral particles, which are not that closely related to the electrical plasma properties, will be discussed in the next section.

3.2 Influence of the pressure on the plasma densities

The densities of the charged particles are, of course, very determining for the plasma characteristics, but since in spectroscopic applications dissociation and excitation are the key elements, one also has to study the behavior of the excited species present in the plasma. In Fig. 4 the spatially averaged densities of He^{**}, $He_m{}^*$ and $He_2{}^*$ are plotted as a function of pressure. The pressures range from 25 to 1100 mbar. $He_m{}^*$ is clearly the most important excited helium-state in the entire range with values ranging from 1.7×10^{18} m^{-3} to 3.6×10^{18} m^{-3}, at pressures of 300 mbar and 1100 mbar, respectively. This is rather high in comparison to He^{**}, where the densities range from 1.4×10^{16} m^{-3} to 4.2×10^{17} m^{-3}, and $He_2{}^*$, which is characterized with densities ranging from 2.6×10^{14} m^{-3} to 8.3×10^{17} m^{-3}.

In Fig. 5, the spatially averaged densities of the charged particles are shown for the same pressure range as in Fig. 4. In this figure, it is seen that $He_2{}^+$ is the most important positive ion in the entire pressure range. Only in the region from 50 to 140 mbar, where the plasma activity seems to be higher, there is about 30% contribution of He^+ to the total positive charge density. Outside this region, $He_2{}^+$ almost completely dominates the positive charge.

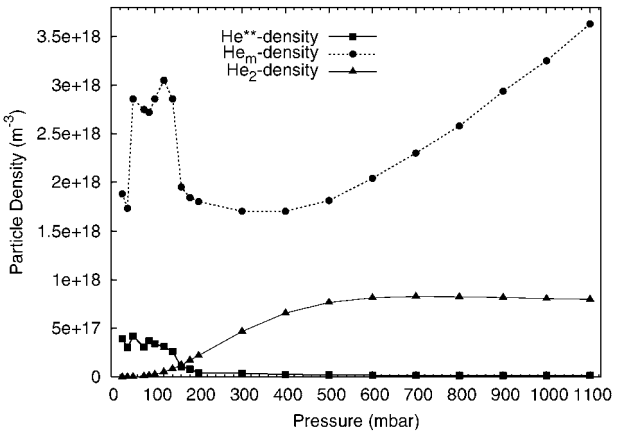

Fig. 4 Calculated spatially averaged neutral particle densities at the maximum positive current for pressures ranging from 25 to 1100 mbar.

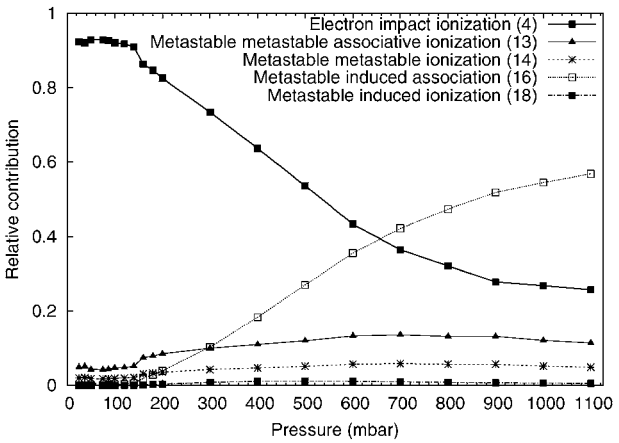

Fig. 6 Calculated relative contributions of the chemical reactions leading to the destruction of He_m^*.

Fig. 4 and Fig. 5 show that all plasma species, except for He_2^*, exhibit a significantly higher density in the range from 50 to 140 mbar. It is remarkable how the increase of the pressure has a different effect on different species: He_m^* exhibits the most spectacular rise in density as a function of pressure. The He_2^+ and the electron densities also show a rise, but it is less steep. The He^+ and the He^{**} densities appear to decrease as a function of pressure and the He_2^* densities become independent of He pressure above *ca.* 500 mbar. In the following we will study this behavior in more detail to identify the governing processes in the discharge. Therefore, we calculated the relative contributions of the chemical reactions to the total production and destruction rate of every particle using

$$\alpha_{i,j} = \frac{c_{i,j} R_{i,j}}{\sum_k c_{i,k} R_{i,k}} \qquad (6)$$

where $\alpha_{i,j}$ is the relative contribution of reaction j to the total production or destruction of particle i and $R_{i,j}$ is the spatially averaged reaction rate of reaction j that influences the density of particle i and is defined by

$$R_{i,j} = k_j \prod_p n_p \qquad (7)$$

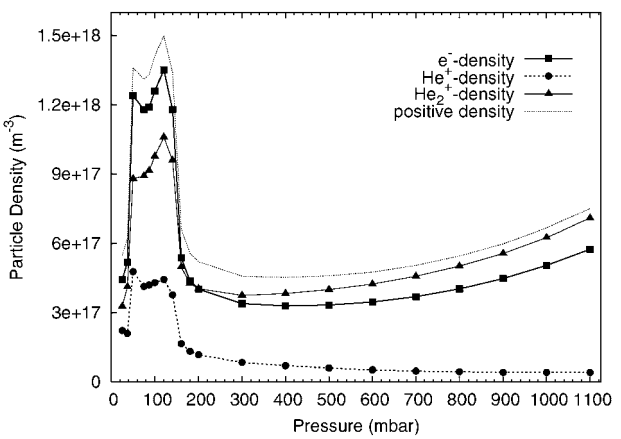

Fig. 5 Calculated spatially averaged charged particle densities at the maximum positive current for different pressures.

where k_j is the reaction rate coefficient and n_p the density of a reacting particle.

The coefficient $c_{i,j}$ in eqn (6) is the associated stoichiometric number that accounts for the amount of particles i that are lost or created in reaction j. Subsequently these relative contributions will be compared with the absolute reaction rates. Hence, a thorough insight in the underlying chemical mechanisms can be obtained.

3.2.1 He_m^*. For every pressure it is calculated from eqn (6) and (7) that the relative contribution of the electron impact excitation from ground state helium (reaction 1) to the total production of He_m^* is more than 93%. Therefore, the production of He_m^* is completely governed by this reaction. The relative contributions of the different reactions leading to the destruction of He_m^* are presented in Fig. 6. This figure clearly shows that at pressures below 650 mbar the electron impact ionization (reaction 4) is the most important reaction in the destruction of He_m^*. At pressures above 650 mbar metastable induced association (reaction 16) becomes the dominating reaction. Indeed, this reaction occurs with 2 He atoms, so it is logical that the rate increases with the He pressure. The other destruction processes are of minor importance in the entire pressure range investigated.

The study of the relative contributions can only tell *which* process is important and not *how* important it is. To obtain information on the absolute importance of a reaction, the absolute reaction rates also need to be studied. Therefore, we present in Fig. 7 the absolute reaction rates of the most important reactions in the discharge. The electron impact excitation (reaction 1), which completely governs the production of He_m^*, appears to be one of the two most important reaction mechanisms in the discharge. Fig. 7 shows that for pressures above 160 mbar the electron impact excitation (reaction 1), is the most important reaction in the discharge and that for pressures below 160 mbar this reaction is the second most important reaction, after the Hornbeck–Molnar associative ionization (reaction 12).

The electron impact ionization (reaction 4) and the metastable induced association (reaction 16) do not attain values higher than 5×10^{17} cm^{-3} s^{-1}. This is much lower than the

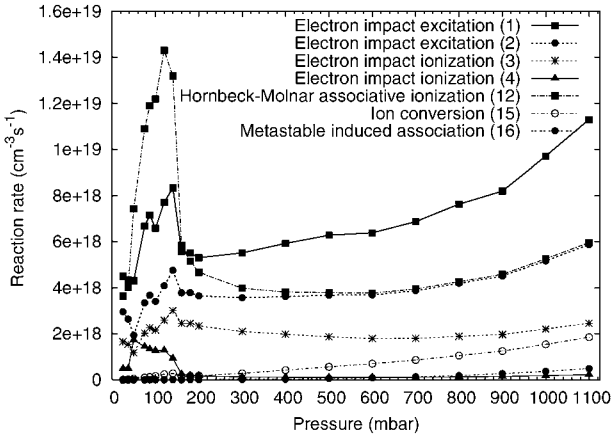

Fig. 7 Calculated spatially averaged reaction rates of the seven most important reactions in the plasma.

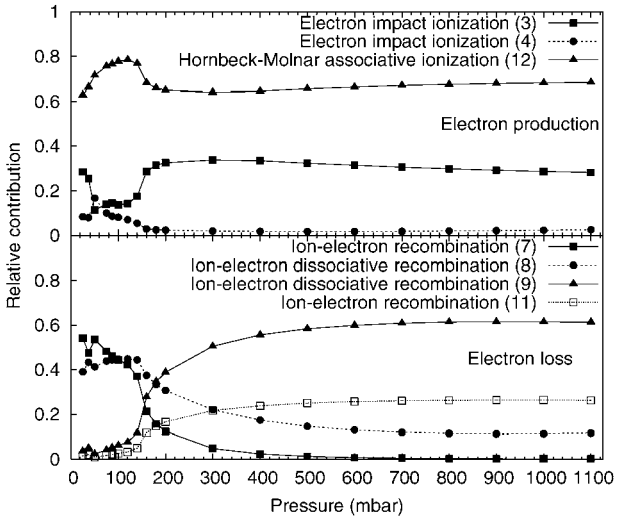

Fig. 8 Calculated relative contributions of the chemical reactions leading to the production and destruction of the electrons.

electron impact excitation rates (reaction 1), as can be seen in Fig. 7. Therefore the two important He_m^* destruction reactions are negligible in comparison with the He_m^* production reaction. In Table 1, it can be seen that the electron impact excitation reaction is directly dependent on the He background gas pressure. This causes the rate of this reaction to steeply rise as a function of pressure, as can be seen in Fig. 7. It also explains the same steep rise of the He_m^* densities in Fig. 4, since the He_m^* densities are completely governed by the electron impact excitation (reaction 1).

In Fig. 7, we also see that in the region from 50 to 140 mbar the Hornbeck–Molnar associative ionization (reaction 12) is clearly the dominant process in the discharge. This reaction boosts up the production of the He_2^+ ions and the electrons. Subsequently, the newly created electrons will produce He_m^* excited states through electron impact excitation (reaction 1). This explains the higher He_m^* density in the region from 50 to 140 mbar that can be seen in Fig. 4. The Hornbeck–Molnar associative ionization (reaction 12) appears to be responsible for the higher plasma activity in the range from 50 to 140 mbar.

3.2.2 The electrons. In Fig. 8, we present the results calculated from eqn (6) for the relative contributions of the chemical reactions leading to the production (top frame) and loss (bottom frame) of the electrons. In the top frame of Fig. 8 it can be seen that Hornbeck–Molnar associative ionization (reaction 12) contributes for 60 to 80% to the production of the electrons at every pressure. Also, electron impact ionization (reaction 3) has a significant influence ranging from 15 to 35% in the entire pressure range.

In the bottom frame of Fig. 8 the relative contributions of the chemical reactions leading to the loss of the electrons are shown. For pressures below 160 mbar the ion–electron recombination (reaction 7) and the ion–electron dissociative recombination (reaction 8) both have relative contributions of about 40 to 50%. For pressures above 160 mbar the loss of the electrons appears to be governed by the ion–electron dissociative recombination (reaction 9), the ion–electron recombination (reaction 11) and the ion–electron dissociative recombination (reaction 8).

For every pressure, none of the above mentioned loss processes attains a reaction rate value above 1.7×10^{17} cm^{-3} s^{-1}. These rates are negligible in comparison with the electron production rates shown in Fig. 7 for Hornbeck–Molnar associative ionization (reaction 12) and electron impact ionization (reaction 3). As a consequence Hornbeck–Molnar associative ionization is the reaction with the largest influence on the electron densities. In Fig. 7, the Hornbeck–Molnar associative ionization (reaction 12) shows very high reaction rates in the range from 50 to 140 mbar. This behavior causes the high electron densities in that same pressure range. For higher pressures, the Hornbeck–Molnar associative ionization (reaction 12) also shows a rise in Fig. 7 similar to the electron impact excitation (reaction 1), but it is less steep. This explains why the rise of the electron densities for higher pressures (shown in Fig. 5) is less steep than the rise of the He_m^* densities shown in Fig. 4.

For every pressure the influence of the Hornbeck–Molnar associative ionization on the electron densities is found to be very important. For the electrons it is shown that the high electron densities in the range from 50 to 140 mbar are directly caused by the Hornbeck–Molnar associative ionization (reaction 12).

3.2.3 He_2^+. The relative contributions of the different reactions to the production and destruction of He_2^+ calculated from eqn (6) are presented in Fig. 9. The top and bottom frame show the relative contributions to the production and destruction of He_2^+, respectively. The Hornbeck–Molnar associative ionization (reaction 12) is again clearly the most important production reaction. However, for higher pressures the ion conversion (reaction 15) also attains relative contributions of about 10 to 20%. The bottom frame in Fig. 9 shows that the destruction of He_2^+ is completely governed by ion–electron dissociative recombination (reactions 8 and 9) and the ion–electron recombination (reaction 11). These three He_2^+ destruction reactions are already discussed above as electron

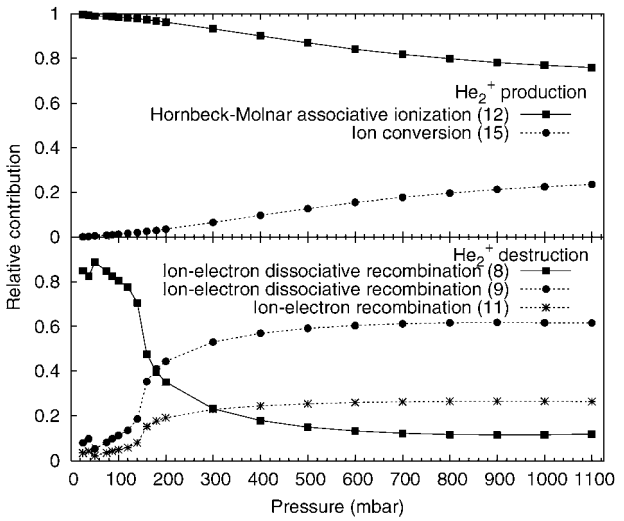

Fig. 9 Calculated relative contributions of the different chemical reactions leading to the production and destruction of the He_2^+ ions.

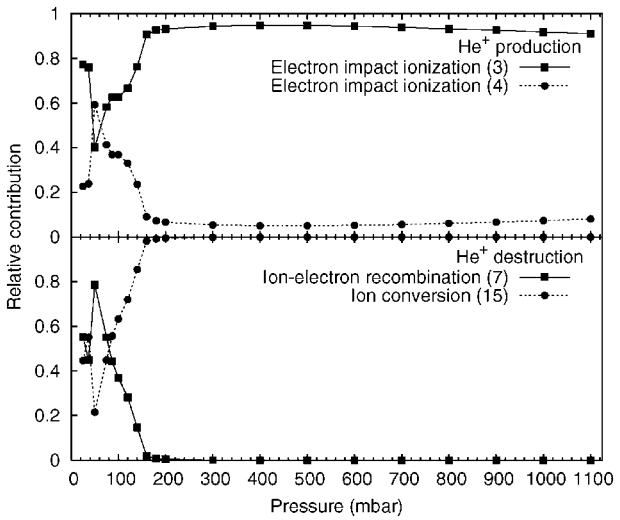

Fig. 10 Calculated relative contributions of the different chemical reactions leading to the production (top frame) and destruction (bottom frame) of He^+ ions.

loss processes and have been found negligible in comparison with the reactions shown in Fig. 7.

The Hornbeck–Molnar associative ionization (reaction 12) and the ion conversion (reaction 15) are both shown in Fig. 7. It is already stated that Hornbeck–Molnar associative ionization is clearly the most important He_2^+ production process. Therefore, the higher reaction rates of Hornbeck–Molnar associative ionization in the range from 50 to 140 mbar (see Fig. 7) are directly responsible for the higher He_2^+ densities in that pressure range.

The rise of the He_2^+ densities as a function of pressure (see Fig. 5), is mostly governed by the Hornbeck–Molnar associative ionization. However, since the ion conversion (reaction 15) shown in Fig. 7 rises more clearly as a function of pressure, it attains a larger contribution in the production of He_2^+ (see Fig. 9). Since the rise of the ion conversion (reaction 15) as a function of pressure is higher than the rise of Hornbeck–Molnar associative ionization, the He_2^+ densities also obtain a steeper rise as a function of pressure, compared to the electron densities.

3.2.4 He^+. In Fig. 10, the results calculated with eqn (6) for the relative contributions of the different reactions leading to the production (top frame) and the destruction (bottom frame) of He^+ are presented at pressures ranging from 25 to 1100 mbar. This figure shows that the production of He^+ is completely governed by the electron impact ionization from ground state He (reaction 3) for almost every pressure. The destruction of He^+, shown in the bottom frame, is completely governed by the ion conversion (reaction 15), except for pressures below 100 mbar.

In Fig. 5, it is shown that the He^+ ions also have a higher density in the range from 50 to 140 mbar, but for higher pressures these densities seem to drop. The higher densities of He^+ in the range from 50 to 140 mbar are due to the higher reaction rates of the electron impact ionization from the He_m^* particles (reaction 4, shown in Fig. 7). The influence of the destruction reactions is small at low pressures, since their rates stay below 1.7×10^{17} cm^{-3} s^{-1}. The high reaction rate of the electron impact ionization (reaction 4) at low pressure is due to the increased He_m^* and electron densities in that range (shown in Fig. 4).

The decrease of the He^+ density as a function of pressure is due to the main destruction process, namely the ion conversion (reaction 15). Fig. 10 shows that at higher pressures the electron impact ionization of the He ground state (reaction 3) is the main He^+ production reaction and also that the ion conversion (reaction 15) is the main He^+ loss reaction. In Fig. 7, it is shown that the electron impact ionization (reaction 3) does not significantly rise as a function of pressure. The ion conversion (reaction 15), however, shows a significant rise as a function of pressure. Since the main production process does not show much influence of pressure and the main destruction process shows a significant rise, the He^+ densities shown in Fig. 4 decrease as a function of pressure.

3.2.5 He_2^*. In Fig. 4, the spatially averaged densities of He_2^* for pressures ranging from 25 to 1100 mbar are shown. This figure shows the He_2^* densities at maximum current density, ranging from 0.1 to 0.3 A cm^{-2}, depending on pressure. At the given moments in time, the current density is very much determined by the conduction current and does not necessarily coincide with the maximum densities of the neutral particles. He_2^* is the only plasma species that does not achieve a maximum density at the maximum current. Indeed, He_2^* is much more important in the afterglow of the discharge. Therefore, to study the influence of the pressure on the He_2^* density, we present in Fig. 11 the He_2^* densities and the rates of the important production and destruction processes as a function of pressure at a later time in the discharge (about 15 μs later). Fig. 11 clearly shows that at a later time in the discharge He_2^* becomes a very important plasma species. It is also shown that the He_2^* densities rise steeply as a function of pressure. This rise is due to the metastable induced association (reaction 16) shown in Fig. 11. The relative contribution of the

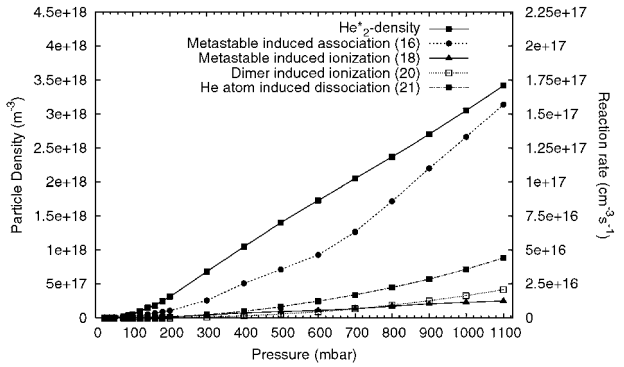

Fig. 11 Maximum values of the calculated spatially averaged densities of He_2^* and the reaction rates of the most important production and destruction reactions.

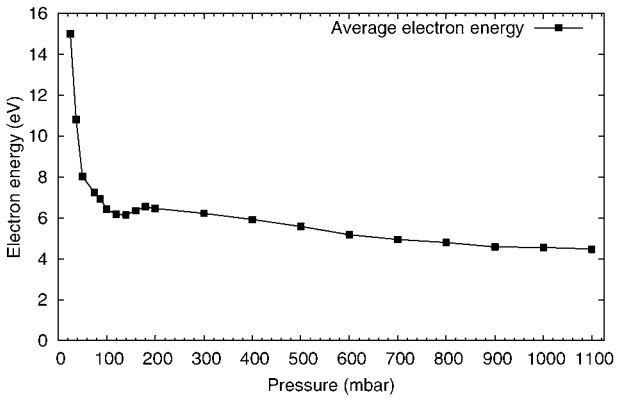

Fig. 12 Calculated average electron energy at maximum positive current for the different calculated pressures.

metastable induced association (reaction 16) to the production of He_2^* is more than 86% for every pressure. The three processes that govern the destruction of He_2^* are also shown in Fig. 11. These are the metastable induced ionization (reaction 18), the dimer induced ionization (reaction 20) and the He atom induced dissociation (reaction 21). Fig. 11 shows that the metastable induced association (reaction 16) is also much more important than these destruction processes. This reaction has a great dependency on the He background gas pressure (see Table 1), which explains the steep rise as a function of pressure. Therefore also the He_2^* densities show a steep rise as a function of pressure.

3.2.6 He^{**}. It can be seen in Table 1 that the electron impact excitation (reaction 2) and the Hornbeck–Molnar associative ionization (reaction 12) are the sole processes where He^{**} is involved, therefore the production and destruction of this particle is completely governed by these two reactions. Fig. 4 shows that the He^{**} atoms only attain significant densities at pressures below 150 mbar. Hence, it appears that for pressures above 150 mbar the Hornbeck–Molnar associative ionization (reaction 12) completely suppresses the production of He^{**}.

It appears that the higher plasma activity in the range from 50 to 140 mbar is closely related to the He^{**} densities and the associated Hornbeck–Molnar associative ionization reaction. Fig. 7 shows that the Hornbeck–Molnar associative ionization has a reaction rate that is almost twice the rate of the second most important reaction in that pressure range. It is shown above that the high densities in that pressure range of the two most important charge carriers He_2^+ and the electrons are also directly related to this reaction. Subsequently, the densities of the other plasma species are directly influenced by these newly formed charge carriers.

These He^{**} densities are rather low for every pressure, but they appear to play a crucial role in the mechanisms of the discharge.

3.3 The stability of the discharge

In ref. 6, it is stated that in this experimental configuration any kind of noble gas with pressures from 10 to 180 mbar can be ignited and sustained. Our calculations show that in the range from 50 to 140 mbar the plasma is significantly more active, as can be seen in the profile of the current densities which are three times as high (see Fig. 2) and in the profiles of the plasma densities, which are also clearly higher in that range (see Fig. 4 and 5). This observation appears to confirm the choice of operating pressures made in ref. 6.

However, the pressure range in which a merely stable discharge can be obtained appears to be much larger in our calculations. Indeed our calculations show that a stable discharge can be obtained with pressures ranging from about 15 mbar to about 1.1 bar. The reasons for the lower and upper limit are evident. Below the pressure of 15 mbar the He background gas density is too low. Therefore there are not enough collision reactions to create a stable plasma. This effect is shown in Fig. 12, where we present the average electron energy at maximum current as a function of pressure. This figure shows that at low pressures there are not enough collisions for the electrons to lose energy, and therefore at lower pressures the energy becomes higher and higher.

Above the pressure of 1.1 bar there are too many He background gas atoms, which causes the electrons to lose too much energy in collisions with He particles. Therefore the electron energy becomes too low and they are not able to perform enough ionization reactions to create a stable plasma.

This effect is also shown in Fig. 12, where it can be seen that at high pressures the electron energy becomes very low and eventually too low to sustain a plasma.

4. Conclusion

We have applied a fluid model to describe a dielectric barrier discharge that has been developed as a new plasma source for analytical spectrometry[6] and we have investigated the influence of the background gas pressure. A helium chemistry was considered based on 7 different species, *i.e.* He background gas atoms, electrons, He_m^* metastable states, He^{**} higher excited states, He_2^* excimers, the atomic ions He^+ and the molecular ions He_2^+. We have also implemented 21 chemical reactions to account for the production and destruction processes of these particles.

The model is applied for the same gap distance (960 μm), dielectric thickness (20 μm), dielectric nature (glass), voltage

amplitude (750 $V_{peak\text{-}to\text{-}peak}$) and voltage frequency (5 kHz) as is common for this plasma source.

Our results show that for this configuration in the region from 50 to 140 mbar the plasma current density is three times as high as outside this pressure range and that the electrons, the ions and the excited species, except for the He_2^* excimers, also have a distinctly higher density. This shows that for pressures from 50 to 140 mbar there is a higher plasma activity. This appears to be in agreement with the typical operating conditions of 10 to 180 mbar used in experiments.[6]

Our calculated stability range is however larger than 50 to 140 mbar. Stable discharges were obtained at pressures ranging from about 15 mbar to about 1.1 bar. The lower pressure limit is due to the lack of background gas atoms available for collision in the discharge. The upper pressure limit is due to the loss of the electron energy in collisions with the background gas, resulting in too low electron energies to sustain the plasma.

In order to obtain information on the discharge regime, we also investigated the spatial distributions of the potential and the charge densities. For two very different cases, glow-like profiles with distinct positively charged sheaths and quasi-neutral plasma bulks were obtained.

The high plasma activity in the pressure range from 50 to 140 mbar has been found to be closely related to the Hornbeck–Molnar associative ionization reaction (reaction 12). Our calculations show that this reaction clearly has the highest rate in the pressure range from 50 to 140 mbar. The two most important charge carriers, He_2^+ and the electrons, are directly formed by this reaction and subsequently these species determine the formation of the other plasma species. The calculations therefore show that, although He^{**} has a low density in the discharge, it is an important source for the governing Hornbeck–Molnar associative ionization.

The operating pressure is not the only parameter that can be subjected to study. The applied voltage amplitude, voltage profile, applied frequency, geometrical effects and the power determine the discharge properties and are interesting subjects for future research. Also, operating the discharge with other discharge gases, such as argon, is interesting for future study, since the discharge gas is a determining stability factor, but of course is also an important cost factor, which must not be forgotten.

References

1 J. C. T. Eijkel, H. Soeri and A. Manz, *J. Anal. At. Spectrom.*, 2000, **15**, 7–300.
2 D. C. Liang and M. W. Blades, *Spectrochim. Acta, Part B*, 1989, **44**, 1049–1057.
3 A. M. Bilgic, E. Voges, U. Engel and J. A. C. Broekaert, *J. Anal. At. Spectrom.*, 2000, **15**, 579–580.
4 Y. Yin, J. Messier and J. A. Hopwood, *IEEE Trans. Plasma Sci.*, 1999, **27**, 1516–1524.
5 W. C. Davis and R. K. Marcus, *J. Anal. At. Spectrom.*, 2001, **16**, 931–937.
6 M. Miclea, K. Kunze, G. Musa, J. Franzke and K. Niemax, *Spectrochim. Acta, Part B*, 2001, **56**, 37–43.
7 J. A. C. Broekaert, *Anal. Bioanal. Chem.*, 2002, **374**, 182–187.
8 J. Franzke, K. Kunze, M. Miclea and K. Niemax, *J. Anal. At. Spectrom.*, 2003, **18**, 802–807.
9 V. Karanassios, *Spectrochim. Acta, Part B*, 2004, **59**, 909–928.
10 K. Kunze, M. Miclea, G. Musa, J. Franzke, C. Vadla and K. Niemax, *Spectrochim. Acta, Part B*, 2002, **56**, 137–146.
11 M. Miclea, K. Kunze, J. Franzke and K. Niemax, *Spectrochim. Acta, Part B*, 2002, **57**, 1585–1592.
12 K. Kunze, M. Miclea, J. Franzke and K. Niemax, *Spectrochim. Acta, Part B*, 2003, **58**, 1435–1443.
13 J. R. Roth, *Industrial plasma engineering: Volume 1: Principles*, IOP Publishing Ltd, Philadelphia, 1995.
14 B. Eliasson and U. Kogelschatz, *IEEE Trans. Plasma Sci.*, 1991, **19**, 309–323.
15 F. Massines and G. Gouda, *J. Phys. D: Appl. Phys.*, 1998, **31**, 3411–3420.
16 O. Goossens, E. Dekempeneer, D. Vangeneugden, R. V. de Leest and C. Leys, *Surf. Coat. Technol.*, 2001, **142**, 474–481.
17 U. Kogelschatz, *Plasma Sources Sci. Technol.*, 2002, **11**, A1–A6.
18 G. Hagelaar, Modeling of microdischarges for display technology, *PhD thesis*, Technische Universiteit Eindhoven, 2000.
19 G. J. M. Hagelaar, G. M. W. Kroesen, U. van Slooten and H. Schreuders, *J. Appl. Phys.*, 2000, **88**, 2252–2262.
20 W. J. M. Brok, J. van Dijk, M. D. Bowden, J. J. A. M. van der Mullen and G. M. W. Kroesen, *J. Phys. D: Appl. Phys.*, 2003, **36**, 1967–1979.
21 W. J. M. Brok, M. F. Gendre and J. J. A. M. van der Mullen, *J. Phys. D: Appl. Phys.*, 2007, **40**, 156–162.
22 E. Wagenaars, R. Brandenburg, W. J. M. Brok, M. D. Bowden and H. E. Wagner, *J. Phys. D: Appl. Phys.*, 2006, **39**, 700–711.
23 T. Martens, A. Bogaerts, W. J. M. Brok and J. van Dijk, *Anal. Bioanal. Chem.*, 2007, in press.
24 C. Punset, J. P. Boeuf and L. C. Pitchford, *J. Appl. Phys.*, 1998, **83**, 1884–1897.
25 J. D. P. Passchier and W. J. Goedheer, *J. Appl. Phys.*, 1993, **74**, 3744–3751.
26 F. Massines, A. Rabehi, P. Decomps, R. B. Gadri, P. Ségur and C. Mayoux, *J. Appl. Phys.*, 1998, **83**, 2950–2957.
27 Y. B. Golubovskii, V. A. Maiorov, J. Behnke and J. F. Behnke, *J. Phys. D: Appl. Phys.*, 2003, **36**, 39–49.
28 L. Mangolini, C. Anderson, J. Heberlein and U. Kortshagen, *J. Phys. D: Appl. Phys.*, 2004, **37**, 1021–1030.
29 G. J. M. Hagelaar and L. C. Pitchford, *Plasma Sources Sci. Technol.*, 2005, **14**, 722–733.
30 H. W. Ellis, R. Y. Pai, E. W. McDaniel, E. A. Mason and L. A. Viehland, *At. Data Nucl. Data Tables*, 1976, **17**, 177–210.
31 R. C. Reid, J. M. Prausnitz and B. E. Poling, *The properties of gases and liquids*, McGraw-Hill, New York, 1987.
32 R. A. Svehla, Estimated viscosities and thermal conductivities of gases at high temperatures, *Technical Report, R-132*, NASA, 1962.
33 S. Rauf and M. J. Kushner, *J. Appl. Phys.*, 1999, **85**, 3460–3469.
34 A. V. Vasenkov and M. J. Kushner, *Phys. Rev. E: Stat. Phys., Plasmas, Fluids, Relat. Interdiscip. Top.*, 2002, **66**, 066411.
35 The Siglo Database, CPAT and Kinema Software, http://www.siglo-kinema.com.
36 R. K. Janev, W. D. Langer, D. E. J. Post and K. J. Evans, *Elementary processes in hydrogen-helium plasmas. Cross sections and reaction rate coefficients*, Springer-Verlag, Berlin, Heidelberg, New York, 1987.
37 R. Deloche, P. Monchicourt, M. Cheret and F. Lambert, *Phys. Rev. A*, 1976, **13**, 1140–1176.
38 P. Zhang and U. Kortshagen, *J. Phys. D: Appl. Phys.*, 2006, **39**, 153–163.
39 J. Stevefelt, J. M. Pouvesle and A. Bouchoule, *J. Chem. Phys.*, 1982, **76**, 4006–4015.
40 J. P. Boeuf, presentation at *Master Class: Microplasmas*, Bad Honnef, Germany, 13–15 Oct. 2005.
41 Y. P. Raizer, *Gas discharge physics*, Springer Verlag, Berlin, 1991.
42 I. Radu, R. Bartnikas and M. R. Wertheimer, *IEEE Trans. Plasma Sci.*, 2003, **31**, 1363–1378.
43 F. Massines, P. Ségur, N. Gherardi, C. Khamphan and A. Ricard, *Surf. Coat. Technol.*, 2003, **174**, 8–14.
44 B. Chapman, *Glow discharge processes*, John Wiley & Sons Inc., New York, 1980.
45 A. Grill, *Cold Plasma in Materials Fabrication: from Fundamentals to Applications*, IEEE Press, New York, 1994.

